Imaging of Subsurface Regions of Random Media by Remote Sensing

Randall L. Barbour, Harry L. Graber, Raphael Aronson*, and Jack Lubowsky

Dept.'s of Pathology and Biophysics, SUNY Health Science Center at Brooklyn, 450 Clarkson Ave., Brooklyn, NY 11203, *Dept. of Physics, Polytechnic University, 333 Jay St., Brooklyn, NY 11201

Abstract

The ability to selectively probe a random medium, even in the limit of isotropic scattering, suggests it should be possible to reconstruct images of a dense scattering medium from the information contained in the backscatter surface emission profile. Consideration of the imaging problem also requires knowledge of the impact that localized absorption at any site in the medium would have on the response of detectors at the surface. By applying the concept of importance used in reactor theory, we have calculated this relationship for various homogeneous media. This information was subsequently incorporated into several image reconstruction algorithms which employ a backprojection strategy. The algorithms were tested by applying them to simulated surface emission profile data for homogeneous scattering media with embedded arrays of black-body absorbers. The algorithms correctly identified the size and location of the arrays, resolved internal structural features, and showed significant improvement upon iteration.

1.0 Introduction

Any type of material which diffusely scatters penetrating radiation can be regarded as a random medium. This constitutes a very large class of materials, including nearly all solid objects and various types of gaseous and liquid turbid media. Types of radiation scattered can include particles (*e.g.*, electrons, neutrons and others), acoustic waves, and most of the electromagnetic spectrum. Materials which diffusely scatter penetrating radiation at one frequency may, of course, be transparent at others. Tissues behave in this manner; they are transparent to X-rays but diffusely scatter visible and near infrared (NIR) light.

In many instances, even though the frequency of interest is intensely scattered, it would nevertheless by of great practical value to identify the internal structure and other properties of the target medium with the scattered frequency. This is the case with tissue at NIR frequencies. At these frequencies, light penetrates deeply into tissue where heme proteins, principally hemoglobin, exhibit oxygen-dependent spectral changes. The utility of monitoring such events stems from the known close association between organ function and oxidative metabolism which, in turn, is closely linked to the oxidation state of heme proteins. Thus, by performing an NIR optical measurement, the physiological vitality of the tissues can be directly and noninvasively measured.

As desirable as such information may be, to generate an optical image of tissue, or of any other type of random medium, requires the solution of a difficult inverse problem. At first glance, this problem may appear intractable, as, at a microscopic level, the random scattering of a photon makes it impossible to specify its path. Knowledge of the path of the detected radiation, however, is critical, as the essence of any imaging method ultimately requires that the detected signal be related to some properties of a specified volume. One strategy which is being considered to address this problem is to employ time-resolved techniques[1-4] which seek to isolate the coherent (unscattered) component of the transmitted or singly backscattered photons. In dense scattering media however, the intensity of the coherent component declines exponentially with distance. Therefore, the intensity of this signal would become vanishingly small for most of the more clinically interesting body structures, such as the trunk, head, arms or legs. In most practical situations the only measurable signal would be that of

0-8194-0521-3/91/$4.00

diffusely scattered radiation. The issue then becomes, is it possible to make use of this signal to yield usable information.

While the occurrence of scattering significantly complicates the imaging process, it uniquely affords the potential for remote sensing. In many clinical situations, particularly in acute care settings, the ability to perform a remote sensing measurement could provide invaluable information. In fact, despite the great utility of current medical imaging modalities (*e.g.*, X-ray computed tomography (X-ray CT), magnetic resonance imaging (MRI) or positron emission tomography (PET)), the need to surround the patient by the device greatly restricts their use in acute care environments. It also requires that these devices constitute large, fixed installations. On the other hand, instrumentation for an optical backscatter measurement could be scaled from nearly a hand-held device to one for whole-body imaging, depending on the intended application.

1.1 Formulation of Imaging Problem

The approach we have taken has been to consider the problem of imaging in random media as comprising three parts. The first is the need to identify a measurement strategy which permits the selective interrogation of a random medium. The second problem is the requirement to quantitatively relate a detected signal to those volumes in the target medium which significantly contribute to a detector response. The third problem addresses how to numerically process this data in order to yield an actual 3-D image of the target medium.

From the outset, we have felt it important to evaluate the likelihood that usable images of targets buried deep in a random medium might be obtained by modeling inexpensive and rugged instrumentation designs (*i.e.*, CW sources and detectors). We wished to examine these conditions first, before considering more expensive and delicate instrumentation designs (*e.g.*, ultrafast lasers with a streak camera), because in many instances, even low resolution images could prove useful. We have chosen to model tissue, initially, as an isotropic scattering medium in the full knowledge that it is not. The utility of this approach is that it permits a simple means of evaluating the limits of image resolution which might be obtained of targets buried deep within tissue. This follows because a) isotropic scattering produces a rapid rate of beam spreading which gives a poor, if not worst-case, scenario for resolving buried targets, and b) the spatial distribution of photons produced by isotropic scattering should approximate that which exists deep within tissue (*i.e.*, that produced by a diffusion process[7]). We also chose to use Monte Carlo methods rather than analytic expressions[5] as the former provides the greatest flexibility for evaluating different measurement strategies.

We do not claim that isotropic scattering is the best model, only that it gives useful information with a minimum of effort. We do believe, however, that it serves as a reasonable starting point in spite of the fact that it is known that photon scattering in tissue is forward directed[6]. The impact of this inconsistency should become less the deeper the photons propagate in tissue (which is the case we are most interested in studying) because, as discussed by Chandrasekhar[8] and by others, in the limit of a large number of collisions an anisotropic process reduces to Brownian motion, or diffusion.

The present study extends preliminary reports in which we demonstrated, for the first time, the feasibility of reconstructing images of objects embedded in a random medium by considering only the diffusely backscattered signal[10-12]. Independently, Singer *et al.* [13] have also reported progress on imaging in diffusing media. While the quality of their images was good, they were considering a much

smaller medium (*i.e.*, number of volume elements) than we have, and made use of intensity readings about the entire surface, not just backscatter signal as we have done.

2.0 Methods

2.1 Derivation of Weight Function

Let Ψ_{ij} = collision density ($cm^{-3}s^{-1}$) in voxel i, due to photons injected into the medium by source j; this is equal to the product of the photon intensity in the voxel ($cm^{-2}s^{-1}$) and the macroscopic total cross-section Σt_i (cm^{-1}). P_{ik} = contribution (*i.e.*, adjoint) to the fluence ($cm^{-2}sr^{-1}$) over a 1-second time interval at detector k, due to a photon source in voxel i isotropically emitting photons into the medium at a rate of 1 s^{-1}. When the medium is illuminated by an external source, the number of photons "born" in the ith voxel each second, Ns_i, is given by:

$$Ns_i = \Psi_{ij} V_i \Sigma s_i / \Sigma t_i \tag{1}$$

where V_i is the volume of the ith voxel, Σs_i is the scattering cross-section for voxel i. The number of photons absorbed in the ith voxel each second, Na_i, is:

$$Na_i = \Psi_{ij} V_i \Sigma a_i / \Sigma t_i \tag{2}$$

where Σa_i is the absorption cross-section for voxel i. Of the Na_i photons absorbed in the ith voxel, a fraction equal to P_{ik} would have been received by detector k if they hadn't been absorbed. That is:

$$(\Delta I_{jk})_i = \Psi_{ij} P_{ik} V_i \Sigma a_i / \Sigma t_i \tag{3}$$

where $(\Delta I_{jk})_i$ is the absolute decrease in the average angular intensity ($cm^{-2}sr^{-1}s^{-1}$) at detector k caused by absorption in voxel i. As we have restricted our attention so far to media in which Σt is constant, the weight (*i.e.*, the strength of the coupling between absorption and detector response) is:

$$w_{ijk} = \Psi_{ij} P_{ik} V_i / \Sigma t \tag{4}$$

2.2 Calculation of Weights by Monte Carlo Simulation

The quantity Ψ_{ij} is readily found by Monte Carlo methods in which photons are injected into the medium by source j and a count is kept of the number of collisions in voxel i. Determination of P_{ik} is not as straightforward; it is not feasible to simulate a medium with an embedded source and count the number of photons exiting in the field of view of detector k, as a large number of simulations would be required and the detectors would have to cover a fairly large surface area and a large solid angle. Calculation of P_{ik} becomes a much more tractable problem when one employs a reciprocity theorem of radiation transport theory[14]:

$$G(\mathbf{r}_1,\Omega_1;\mathbf{r}_2,\Omega_2) = G(\mathbf{r}_2,-\Omega_2;\mathbf{r}_1,-\Omega_1) \tag{5}$$

where $G(\mathbf{r}_1,\Omega_1;\mathbf{r}_2,\Omega_2)$ is the angular intensity at the point $\mathbf{r}_1$ in direction Ω_1, due to photons born, at a rate of 1 s^{-1}, at $\mathbf{r}_2$ in direction Ω_2. For a detector on the surface, at distance R_k from the source and direction Ω_k, the contribution to the fluence per second from photons born at point $\mathbf{r}$ in the medium is

$$P_k(\mathbf{r}) = (1/4\pi)\int_{4\pi} G(R_k,\Omega_k;\mathbf{r},\Omega)d\Omega$$
$$= (1/4\pi)\int_{4\pi} G(\mathbf{r},-\Omega;R_k,-\Omega_k)d\Omega$$
$$= (1/4\pi)\int_{4\pi} G(\mathbf{r},\Omega;R_k,-\Omega_k)d\Omega \quad (6)$$

and the integral in eq. 6 is the intensity at **r**, due to a single photon launched into the medium along the detector axis. Monte Carlo methods can be used to calculate the average number of collisions in each voxel i per photon injected into the medium from the source, F_{ij}, and from the detector, F_{ik}. The strength of source j, S_j (s^{-1}), may be set to any desired value. The equations relating these quantities to Ψ_{ij} and P_{ik} are:

$$\Psi_{ij} = S_j F_{ij}/V_i \quad (7)$$

$$P_{ik} = F_{ik} / 4\pi V_i \Sigma t \quad (8)$$

Substitution of eqs. 7 and 8 into eq. 4 yields:

$$w_{ijk} = S_j F_{ij} F_{ik} / 4\pi V_i \Sigma_t^2 \quad (9)$$

2.3 Image Reconstruction

The expression in eq. 3 gives the reduction in the angular intensity of light measured by detector k caused by the excess absorption in voxel i. (Note that this quantity will be negative if voxel i has an absorption cross-section lower than that in the reference medium used for the calculation of the weight function). If the additional absorption in every voxel is sufficiently small that it does not significantly change the values of F_{ij} and F_{ik} of voxels in its vicinity from their values in the reference medium, then the net reduction in reflected intensity at k is simply:

$$\Delta I_{jk} = (I_0 - I)_{jk} = (4\pi\Sigma t^2)^{-1}\sum_i (F_{ij}F_{ik}\Sigma a_i / V_i) \quad (10)$$

or

$$\Delta I_{jk} = \sum_i (w_{ijk}\Sigma a_i) \quad (11)$$

where I and I_0 are the intensities of backscattered light from the test and reference media, respectively. Every reflectance measurement yields an equation having the form of eq. 11. When the number of source-detector pairs equals the number of voxels, a fully determined system is obtained, in which all elements of the weight matrix **W** and the measurement vector **y** are known:

$$\mathbf{y} = \mathbf{W}\mathbf{x} \quad (12)$$

or

$$\mathbf{W}^{-1}\mathbf{y} = \mathbf{x} \quad (13)$$

In eq. 12 and eq. 13, **y** contains the ΔI_{jk}'s, **W** the w_{ijk}'s, and **x** the Σa_i's. For most problems, the system of eq. 12 will contain at least several thousand equations.

2.3.1 "Unfiltered 'Backprojection'" Algorithm

By drawing an analogy between the straight line paths of X-rays in the X-ray CT imaging problem

and the calculated weight functions, a simple unfiltered backprojection scheme[15] can be formulated. In our system, because there is no unique path taken by photons from source to detector, the ratio I/I_0 is not a simple exponential function of the medium's absorption cross-section. However, the relative darkening $(1 - I/I_0) = v$ clearly is a measure of the effectiveness of the medium's excess absorption in removing light from a detector's field of view. The relative darkening is 0 if no difference exists between the measurements for the unknown and reference media, and is 1 if no light reaches the detector from the unknown medium. The first algorithm used consisted of "backprojecting" the measurements of v_{jk} through the medium for all source-detector pairs, and summing the results. As scattered light may, in principle, traverse any voxel, every voxel received a contribution from each v_{jk}, equal to the product of v_{jk} and w_{ijk}. This procedure alone would always produce an artifact, assigning larger numbers to shallow layers where the weights are higher. To compensate, the sum $\sum_j\sum_k w_{ijk}$ was calculated for each voxel, and the final result, t_i, which is referred to here as an "image density," is the weighted average:

$$t_i = \sum_j\sum_k w_{ijk}v_{jk} \Big/ \sum_j\sum_k w_{ijk} \tag{14}$$

2.3.2 Iterative Backprojection

Once an estimate of the image density has been made, an estimate of the relative darkenings may be calculated, and compared to the measured values:

$$u_{jk} = \sum_i w_{ijk}t_i \Big/ \sum_i w_{ijk} \tag{15}$$

where t_i is the image density in the ith voxel and u_{jk} is the calculated relative darkening. If the image is an accurate representation of the medium, u_{jk} and v_{jk} are equal. If $u_{jk} \neq v_{jk}$, the difference between them is a measure of the error in the image density estimates. A "difference image" is calculated by backprojecting the quantity $(u_{jk} - v_{jk})$, and calculating a correction, Δt_i, as:

$$\Delta t_i = \sum_j\sum_k w_{ijk}(u_{jk} - v_{jk}) \Big/ \sum_j\sum_k w_{ijk} \tag{16}$$

The corrected image density then is $t_i' = t_i - \Delta t_i$. When substituted into eq. 15, it yields an improved estimate of u_{jk}. The process can continue until all $(u_{jk} - v_{jk})$'s are made arbitrarily close to 0.

2.3.3 Sequential Iterative Backprojection

As source-detector pairs with small separations R have much larger fractions of the total weight in the layers near the surface than do those with larger R, they should be regarded as giving more reliable information on the absorption cross-sections in those layers. The implication for image reconstruction is that the number of iterations needed may be reduced if the algorithm begins by backprojecting only the measured v_{jk}'s for small-R source-detector pairs, and iterating until a convergence criterion near the surface is met. Measurements for successively greater values of R would then be included, and additional iterations performed to reconstruct the image in successively deeper regions.

2.4 Monte Carlo Methods

All simulations modeled photons as particles undergoing isotropic scattering in a medium having a

zero or non-zero absorption cross-section. The scoring functions used, the equations which determined the intercollision distance and the post-scattering direction, and techniques used to maximize the efficiency of the calculation have all been reported elsewhere[10].

In simulation of reflectance measurements for the imaging studies the model medium was infinitely long and wide, and its thickness was 32 mean free pathlengths (MFP) in one case (cube array absorber) and 10 MFP in another ("T" absorber). The two surfaces were planar and parallel. Photons entered the medium at a single point, normal to the surface. The entire area of the illuminated surface within a radius of 10 MFP of the point of injection was divided into 1 MFP^2 squares. Within each square were eight collimated detectors, each with its central axis oriented at $\Phi = 0°$ with respect to the line joining the point of injection to the center of the detector square. The inclination angles of the detectors were 10°, 20°,..., 80° from the normal. A photon emerging from the medium within one of the 1 MFP^2 squares is received by a detector if the angle between the detector axis and the direction of the photon's final free flight in the medium is $\leq 10°$.

Correlated sampling was employed in these simulations, *i.e.*, the propagating photons were forced to follow identical paths in both the medium to be imaged and in the reference medium. As a consequence, any difference between I and I_0 for a given source-detector pair must be due to the effect of the excess absorption in the medium being imaged.

Collision density calculations were performed by simulating a model medium with the same composition as the corresponding reference medium in the reflectance measurement simulations (cube array absorber: 32 MFP thick, $\Sigma a = 0$; "T" absorber: 10 MFP thick, $\Sigma a = .01\Sigma t$). Photons were injected at a single point on the surface, in a direction corresponding to either a source or the central axis of a detector (cube array absorber: $\Theta = 0°, 10°, 30°, 80°$; "T" absorber: $\Theta = 0°, 10°, 80°$). The number of collisions in each 1 MFP^3 voxel of the medium lying within a 41 MFP x 41 MFP x 20 MFP (cube array) or 41 MFP x 41 MFP x 10 MFP ("T" absorber) volume was scored, and the average number of collisions per photon injected was subsequently calculated.

3.0. Results

Our first significant insight into the imaging problem for random media occurred when, by using Monte Carlo techniques, we demonstrated that even in the limit of isotropic scattering, the overall path of the detected backscattered signal is strongly dependent on the position and orientation of the detector[10,11,16,17]. In other words, although the path of an individually scattered photon cannot be specified, the ensemble average of all paths of photons emerging into a particular detector most certainly can be identified. The spatial distribution of detected photons, in turn, varies with receiver position and orientation. This finding is illustrated in Figure 1, which shows, for two different distances separating source and detector, the dependence of the distribution of maximum penetration depth of detected photons on receiver orientation. The detectors modeled in this case were much more poorly collimated than those used later in image reconstructions, encompassing a range of 30° in Θ and 180° in Φ. These histograms reveal, nevertheless, a pronounced shift toward smaller values of maximum penetration depth as the detector orientation changes from $|\Phi| > 90°$ to $|\Phi| < 90°$, especially when $\Theta > 60°$. This observation directly demonstrated the inherent ability to preferentially probe a random medium by examining the surface emission profile.

The second important consideration was made when one of us (R.A.) noted that the concept of importance[18] used in reactor theory could be applied to quantify the spatial distribution of detected photons for any source-detector configuration. This distribution identifies the effect that an increase or decrease in the absorptivity at a given point in space would have on the intensity of light received by a given detector. If the magnitude of this effect is large, then the point under consideration is said

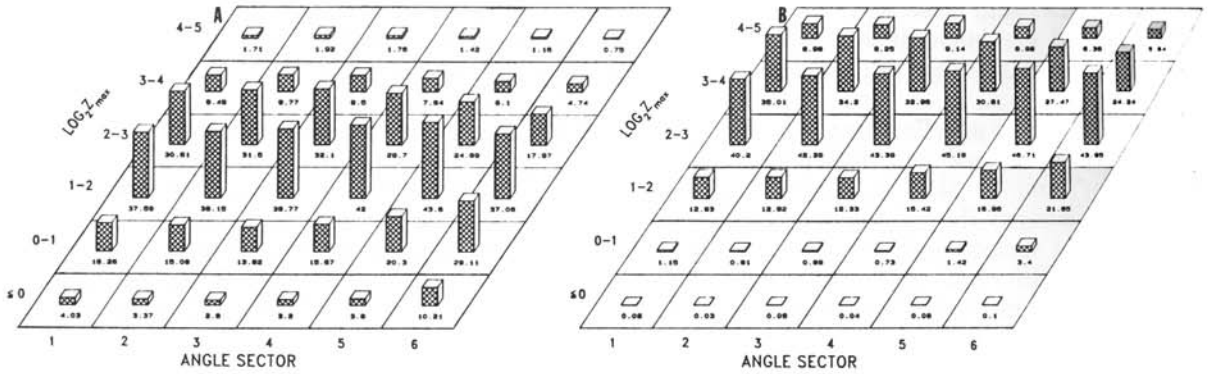

Figure 1: Comparison of depth profiles of maximum depth attained by photons emerging into collimated detectors at distances of 5 MFP (Panel A) and 10 MFP (Panel B) from a collimated point source. Row index is the log (base 2) of the greatest depth attained. Column index is detector orientation (angle sector); 1, Θ = 60-90°, $|\Phi| > 90°$; 2, Θ = 30-60°, $|\Phi| > 90°$; 3, Θ = 0-30°, $|\Phi| > 90°$; 4, Θ = 0-30°, $|\Phi| < 90°$; 5, Θ = 30-60°; $|\Phi| < 90°$; 6, Θ = 60-90°, $|\Phi| < 90°$.

to have a large "weight" for that configuration. The weight function identifies the fractional contribution of each point in space to the detector response for any given source-detector configuration. The idea here was that by calculating weight functions for all source-detector configurations used to measure the backscattered light, inhomogeneities in a random media could not only be detected, but also localized in 3-D space. The dependence of the weight function on distance between source and detector and on detector orientation, for the case of a homogeneous medium, has been reported elsewhere[10]. Examples of contour plots through weight functions calculated for two different types of medium are shown in Figure 2. The medium of 2A was a homogeneous half-space; that of 2B was also a half-space, but containing three layers. A comparison of panels A and B shows that, relative to a homogeneous medium, the presence of multiple layers only monotonically distorts (compresses) the weight function.

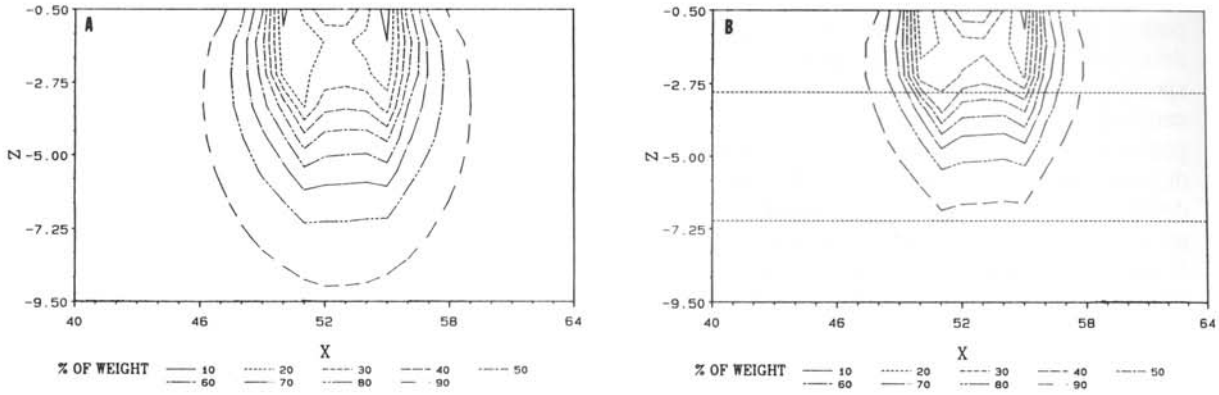

Figure 2: Planar sections through contour surfaces of representative weight functions. For ease of interpretation, voxels were ranked in order of decreasing weight, each weight was converted to percentage of total and contour surfaces drawn about sets of voxels containing first nine deciles of the total weight. Panel A, weight function for homogeneous half-space medium; $\Sigma a/\Sigma t$ = .01, detector orientation-position; R = 5, Θ = 10°, Φ = 0°. Panel B, weight function for 3-layer medium; top layer, $\Sigma a/\Sigma t$ (thickness) = .01 (3); second layer = .05(4); bottom layer = .01(∞). Detector orientation-position same as in Panel A.

The third important step toward developing an imaging algorithm was the realization that an analogy could be drawn between the diffuse spatial distribution of contributing photons, as defined by the weight function, and the straight line paths of X-rays detected in CT scans. Our first attempt at imaging was a modified backprojection scheme similar in concept to that applied in the early years of CT scanning. Using Monte Carlo methods, we simulated measurements of backscattered light propagating in a nonabsorbing, homogeneous, isotropic scattering medium. We chose these because they represented the conditions under which it would be most difficult to resolve buried objects. Our expectation was that if our methods were successful under these conditions, then it would be reasonable to expect that images of even greater resolution could be achieved under more favorable ones. In fact, the conditions that exist in tissue would be more favorable than those modeled here, because tissue is known to exhibit highly forward-directed scattering[6], which retards the rate of beam spreading. In addition, at NIR frequencies tissue is weakly absorbing, thereby further reducing the spread of detected photons.

Schematics of the two heterogeneous absorbers we have attempted to image are shown in Figure 3A. In one case the medium contained an array of eight black cubes. Each of these absorbers measured 2 MFP in length on each edge, and each was located at one of the corners of a 6x6x6 MFP[3] volume. In the second case an absorber having the shape of the letter "T" was modeled. At the depths modeled, neither absorber would be discernible by eye if placed in a real medium. In effect, we wished to play a game of "hide-and-go-seek".

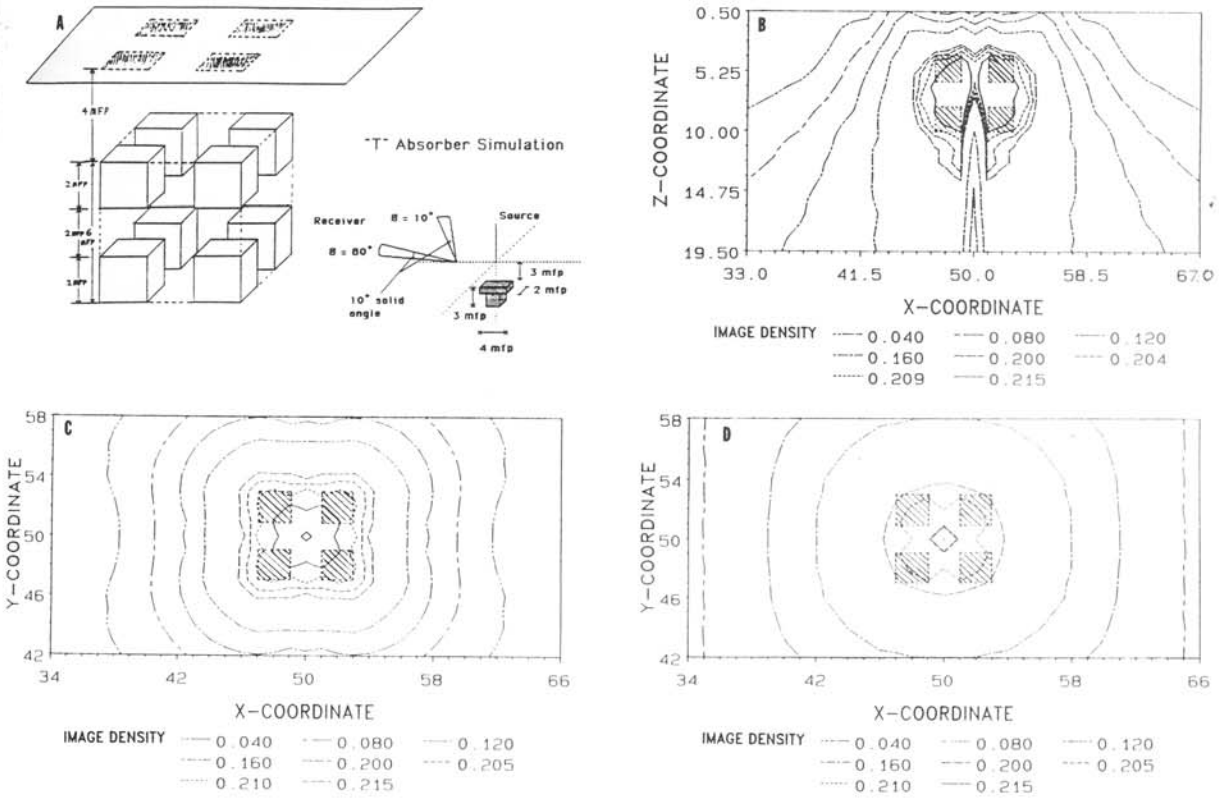

Figure 3. Panel A. Sketch of 8-cubic absorber and "T" absorber arrays modeled in reflectance simulations for imaging studies. Panels B-D, reconstructed images of 8-cubic absorber array by unfiltered backprojection. Panel B, X-Z slice bisecting absorber array. Panel C, X-Y slice at Z = 4-5. Panel D, X-Y slice at Z = 11-12.

The measurement scan was simulated by directing a point collimated source normally to various locations about the surface of the medium (*i.e.*, a raster scan) and measuring the intensity of diffusely backscattered light which entered an array of detectors positioned about each source location. Up to three detector orientations were considered, tilted at angles of 10°, 30° and 80° from the normal, oriented toward the central axis of the source beam, and accepting photons exiting within a cone deviating no more than 10° from the detector axis. The algorithm then calculated the "measured attenuation" and projected it back along the paths in the medium defined by the weight function. As in the original CT algorithm, image reconstruction here was accomplished by the superposition of projected attenuations along paths defined by the weight function from multiple (approximately 100,000) source-detector pairs.

Figure 3B shows a contour plot of the average image density (1.0 being the darkest possible) in a l-MFP-thick slab perpendicular to the medium's surface (X-Z slice) and bisecting the absorber array along one of the main axes. The dotted squares represent the actual spatial location of the absorbing cubes. Inspection of the image reveals that the region of greatest darkening coincides almost precisely with the actual position of the absorbers. Figures 3C and 3D show views of the image from slices parallel to the surface and located 4-5 MFP and 11-12 MFP below the surface. In both cases clear evidence of the expected 4-fold symmetry is observed, and the regions of greatest darkening lie within the boundaries of the simulated absorbers.

Because the results shown in Figure 3 amount to an unfiltered backprojection, the image, as expected, is intensely convolved and exhibits poor contrast. Nevertheless, evidence for having successfully resolved small absorbers (8 MFP^3) buried deeply in a large scattering medium (72,000 MFP^3) is unmistakable.

The next step was to attempt to improve the imaging algorithm by adopting an iterative algebraic deconvolution procedure. The strategy here was to compare each measured attenuation to that calculated for the corresponding source-detector pair from the previous image. The calculated value was defined as the sum, over all voxels, of the product of the weight and image density assigned to the voxels by the previous image. The differences between the calculated and measured attenuations were then backprojected along the weight functions to obtain a difference image. The corrected image is the difference, in every voxel, between the previous image and the difference image, divided by the sum of the weights over all source-detector pairs. Because the difference image also is convolved, one application of this procedure does not produce a correct image. In fact, it is necessary to apply it iteratively until no significant change occurs between successive iterations.

This procedure was applied to an unfiltered backprojection image of the "T" absorber problem. After 18 iteration cycles a comparison of the resultant image to the original unfiltered image revealed an approximate three-fold improvement in contrast (cf. Figure 5) though the rate of convergence was slow.

3.1 Imaging by Sequential Iterative Backprojection

A much faster convergence could be achieved by rearranging the order in which the source-detector pairs were analyzed. The strategy here took into consideration the fact that source-detector pairs which have a greater weight at a given depth in the medium should be regarded as giving more reliable information about the properties at that depth than do other source-detector pairs for which the weight at that depth is less. Thus, while the two previous algorithms had projected the measured attenuation for all source-detector pairs simultaneously, in this version backprojection was performed first for only those pairs having the smallest source-detector spacing, and iterated until the resulting "image" had converged. The algorithm then sequentially considered each successive family of

source-detector pairs located at increasingly greater distances from the sources, and iterated the image for each family until the change in image density in voxels located within approximately 2 MFP of the absorber's true location was reduced to <1% between successive iterations.

Results illustrating the image quality obtained using this algorithm for the "T" absorber problem are shown in Figure 4. Panels A-D represent contours of planar sections through reconstructed images calculated by evaluating detector readings having an orientation of either 10° (Panels A, B) or 80° (Panels C, D) from normal. Comparison of the images generated from the two detector orientations reveal that they differ in image density and location of greatest darkening. These differences, however, are entirely consistent with the differences in the values of the weight functions for the different detector orientations. Inspection of the front and side views reveal the expected asymmetry in image density. The degree of image distortion varies with detector orientation, although this is not unexpected in view of the relatively high noise levels (up to 10%) in some data. Sources of noise include the weight functions, detector readings, and the mis-match in the geometry of the source-detector configurations used to calculate the weight functions (point-collimated sources and detectors) and that actually employed for the simulated measurements (point-collimated sources, 10° conical detectors). Panels E and F show the corresponding sections through an image which is a composite of the individual orientation images superimposed on the actual boundaries of the absorber.

A practical advantage of the sequential iterative scheme is that it yields an "evolving" image. That is, by including increasingly more distant detectors, imaging to greater depths is achieved. Thus, one can select the depth below which improvement in image quality is not considered important. In fact, in order to reduce processing time, this strategy was employed for the images shown in Figure 4. Enhancement in image quality was restricted mostly to the depth of ≤ 4 MFP by

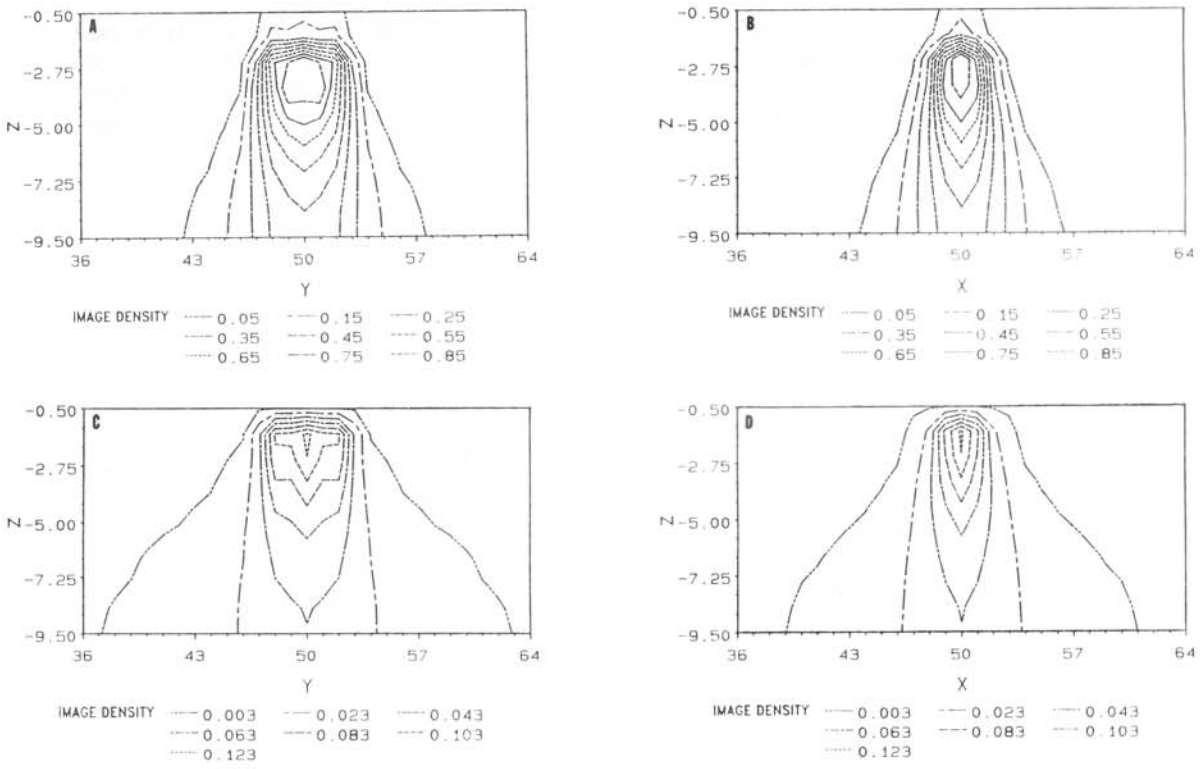

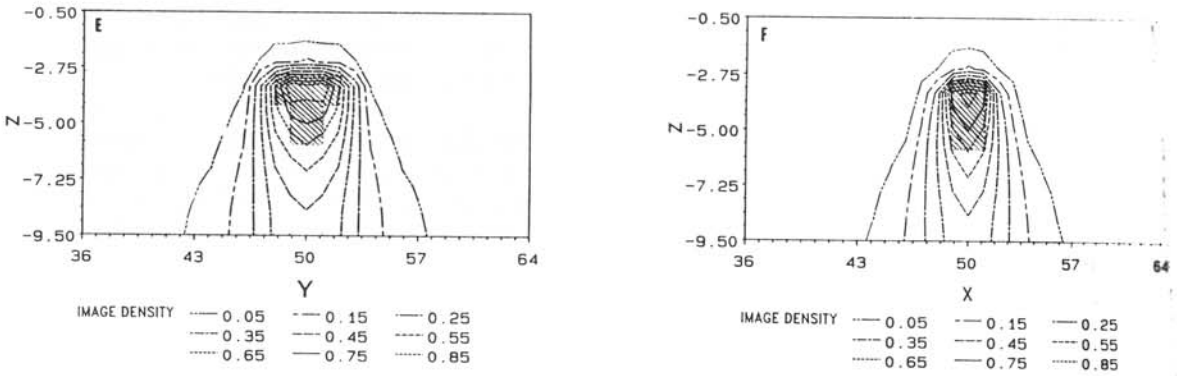

Figure 4. Reconstructed images of "T" absorber using sequential iterative algorithm. Panels A,B; X-Z slice through long and short axis, respectively, of cap using input data from detectors oriented 10° from normal. Panel C, D; same as in Panels A,B except data was from detectors oriented 80° from normal. Panels E,F; composite image calculated by considering data from both detector orientations.

considering only those detectors which preferentially probe within this depth. Thus, only a portion of the available data was considered, and this accounts for the reduction in image quality observed at depths > 4 MFP.

A comparison of the improvement in edge-detection abilities of the three generations of algorithms is shown in Figure 5. In 5A, the ratio of the image density within the cap of the "T" was compared to the portion of each of the three layers lying directly above it. Relative to the first backprojection image, the image density gradient obtained using the sequential iterative scheme was approximately 400 fold greater. A similar comparison was used to quantify the horizontal resolving power of the different algorithms by determining the ratio of image density in each voxel along a line passing through the center of the cap to that within the cap. The results, shown in Figure 5B, demonstrate a much steeper decline in image density when the iterative sequential algorithm was employed.

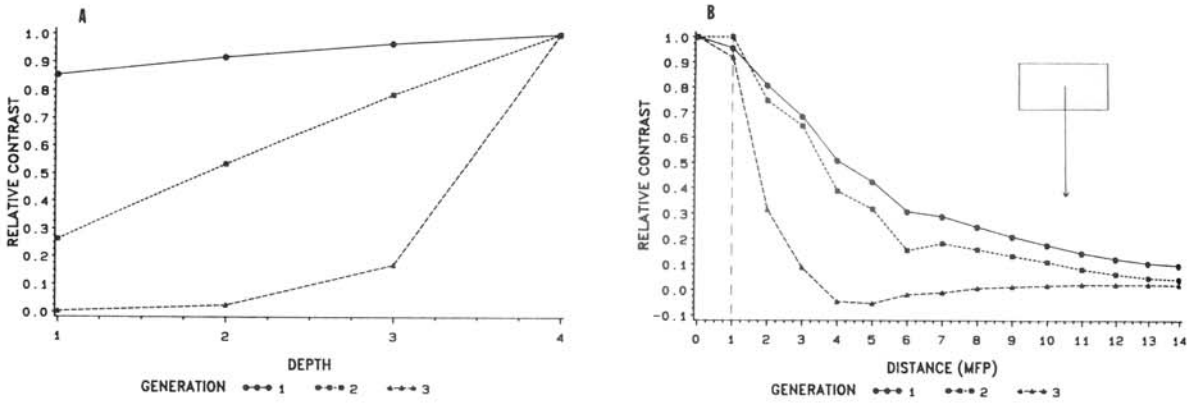

Figure 5. Panel A, comparison of depth resolution by unfiltered backprojection (generation 1), iterative backprojection (generation 2) and sequential iterative backprojection (generation 3) algorithms for "T" absorber problem. Panel B, comparison of horizontal resolution by different imaging algorithms for "T" absorber problem. Dotted line indicates edge of absorber. Sketch indicates direction along which relative contrast vs. distance was examined.

4.0 Discussion

Results presented here, and in recent reports[10-12] are the first to demonstrate the ability to reconstruct images of buried absorbers in random media from analysis of diffusely scattered radiation measured in a remote sensing fashion. The measurement scheme modeled is simple and considers use of CW sources and detectors in a raster type scan. The size of the reconstruction calculation is necessarily much larger than that encountered in problems where the detected radiation is unscattered, as many more voxels must be scored per source-detector configuration and there are many more source-detectors pairs per source location.

Our experience with the sequential iterative algorithm suggests that the amount of computation involved can be significantly reduced if the input data is evaluated in rank-order by proceeding along a "confidence gradient". Another strategy which could complement this approach is suggested in accompanying paper[17]. Comparison of neighboring detectors responses would serve to identify limits on the location and absorptivity of subsurface heterogeneities.

The important task before us is to devise a scheme whereby both the weights and calculated image density can be updated iteratively. This could be accomplished by examining the results obtained with the initial weight estimates and treating regions of heterogeneous absorption as negative-strength sources, thereby accounting for shadow effects which must exist in the vicinity of regions of strong absorption.

5.0 References

1. M.A. Duguay and A.T. Mattick, "Ultrahigh speed photography of picosecond light pulses and echoes," Appl. Opt., 10, pp. 2162-2170, 1971.
2. J.L. Martin, Y. LeCarpentier, A. Antonetti, and G. Grillon, "Picosecond laser stereometry light scattering measurements on biological material," Med. & Biol. Eng. & Comput., 18, pp. 250-252, 1980.
3. B. Chance, J.S. Leigh, H. Miyake, D.S. Smith, S. Nioka, R. Greenfeld, M. Finander, K. Kaufmann, W. Levy, M. Young, P. Cohen, H. Yoshioka, and R. Boretsky, "Comparison of time-resolved and -unresolved measurements of deoxyhemoglobin in brain," Proc. Natl. Acad. Sci. USA, 85, pp. 4971-4975, 1988.
4. J.C. Hebden and R.A. Kruger, "Transillumination imaging performance: A time-of-flight imaging system," Med. Phys., 17, pp. 351-356, 1990.
5. R.F. Bonner, R. Nossal, S. Havlin, and G.H. Weiss, "Model for photon migration in turbid biological media," J. Opt. Soc. Am. A, 4, pp. 423-432, 1987.
6. R. Marchesini, A. Bertoni, S. Andreola, E. Melloni, and A.E. Sichirollo, "Extinction and absorption coefficients and scattering phase functions of human tissues *in vitro*," Appl. Opt., 28, pp. 2318-2324, 1989.
7. M.R. Arnfield, J. Tulip, and M.S. McPhee, "Optical Propagation in Tissue with Anisotropic Scattering," IEEE Trans. Biomed. Eng., 35, pp. 372-381, 1988.
8. S. Chandrasekhar, "Stochastic Problems in Physics and Astronomy," Rev. Mod. Physics, 15, pp. 1ff., 1943.
9. S.T. Flock, B.C. Wilson, and M.S. Patterson, "Hybrid Monte Carlo - diffusion theory modelling of light distributions in tissue," SPIE Laser Interactions with Tissue, 908, pp. 20-28, 1988.
10. R.L. Barbour, H. Graber, J. Lubowsky, and R. Aronson, "Monte Carlo Modeling of Photon Transport in Tissue. V. Model for 3-D Optical Imaging of Tissue," Biophys. J., 57, p. 382a, abst. no. 603, 1990.
11. R. Aronson, R.L. Barbour, J. Lubowsky and H. Graber, "Application of Transport Theory to NIR Medical Imaging", in Modern Mathematical Models in Transport Theory, Berkhauser Press, 1990, in press.
12. R.L. Barbour, H. Graber, R. Aronson, and J. Lubowsky, "Model for 3-D Optical Imaging of Tissue," in proceedings of 10th Annual International Geoscience and Remote Sensing Symposium (IGARSS), vol. II, pp. 1395-1399, 1990.
13. J.R. Singer, F.A. Grünbaum, P. Kohn, and J.P. Zubelli, "Image Reconstruction of the Interior of Bodies that Diffuse Radiation," Science, 248, pp. 990-993, 1990.
14. K.M. Case and P.F. Zweifel, Linear Transport Theory, chap. 1, Addison-Wesley Publishing Co., Reading, 1967.
15. R.A. Brooks and G. DiChiro, "Principles of computer assisted tomography (CAT) in radiographic and radioisotopic imaging," Phys. Med. Biol., 21, pp. 689-732, 1976.
16. R.L. Barbour, H. Graber, J. Lubowsky, and R. Aronson, "Monte Carlo Modeling of Photon Transport in Tissue. I-III." Biophys. J., 57, pp. 381a-382a, abst. no. 599-601, 1990.
17. R.L. Barbour, H. L. Graber, R. Aronson, and J. Lubowsky, "Determination of Macroscopic Optical Properties of Multilayer Random Media by Remote Sensing," SPIE vol. 1431, accompanying paper in these proceedings, 1991.
18. A. Dubi, S.A.W. Gerstl, and D. Dudziak, "Monte Carlo Aspects of Contributons," J. Nucl. Sci. Eng., 68, pp. 19ff., 1978.